Two-Band Model of Super-Regenerative Oscillators

Sergio Sancho, *Senior Member, IEEE*, Almudena Suárez, *Fellow, IEEE*, and Franco Ramírez, *Senior Member, IEEE*

***Abstract*— Super-regenerative oscillators (SROs), based on the switching of an oscillator, enable a high-gain amplification with the advantages of low cost, compact size, and low consumption. These advantages come at the expense of a complex operation, which, in addition to the timescale of the oscillation, involves the timescale of the quench signal. Most previous works describe the SRO with idealized models of the SROs of the Van der Pol type or numerical models valid only under certain conditions. This work presents a new outer tier semianalytical model that accounts for the two timescales by means of a two-band nonlinear formulation. Unlike previous approaches, the new model can predict the dynamic effects associated with the circuit elements in the band of the quench signal. The new formulation identifies the baseband component that determines the oscillator stability properties under the variation of the quench frequency; thus, it provides useful insight into the switched oscillator behavior. The parameters of the two-band model are easily extracted from harmonic balance. The model can be used for a system-level description of the SRO since it can efficiently predict its response under arbitrary input modulations and choices of the frequency and shape of the quench signal. The developed model will be validated through its application to an SRO at 2.8 GHz, which has been manufactured and experimentally characterized.**

***Index Terms*— Envelope transient, harmonic balance, nonlinear model, super-regenerative oscillators (SROs).**

I. Introduction

SUPER-REGENERATIVE oscillators (SROs), switched on and off by a quench signal, take advantage of the exponential growth of the oscillation amplitude during the startup to enable a high-gain amplification [1], [2], [3]. SROs can track modulations in amplitude, frequency, and phase [4], [5], [6], [7]; thus, they may be applied to replace amplifier chains, with the advantages of low cost, compact size, and low consumption, since they are based on a single oscillator element. On the other hand, the works [3], [8], and [9] proposed the application of the switched oscillator for active transponders, making use of the quench signal to modulate the response signal to a frequency modulated continuos wave (FMCW) input. More recently, they have been applied for the implementation of vital sign radar sensors [10], [11], [12] with the advantages of high sensitivity and dc offset and null-point immunity.

Manuscript received 1 March 2023; revised 20 May 2023; accepted 1 July 2023. This work was supported by the Spanish Ministry of Science and Innovation under Project PID2020-116569RB-C31. *(Corresponding author: Sergio Sancho.)*

The authors are with the Departamento de Ingeniería de Comunicaciones, ETSIIT, Universidad de Cantabria, 39005 Santander, Spain (e-mail: sanchosm@unican.es).

Color versions of one or more figures in this article are available at https://doi.org/10.1109/TMTT.2023.3292621.

Digital Object Identifier 10.1109/TMTT.2023.3292621

The quench signal of the SRO (with a much lower frequency than the oscillation) shifts the dominant pair of complex-conjugate poles at the oscillation frequency to the right-hand side (RHS) of the complex plane and back to the left-hand side (LHS) [2]. The oscillation amplitude grows as long as the dominant poles are in the RHS and is extinguished when they shift to the LHS [2]. To obtain the expected high gain, the frequency of the input signal must be close to the oscillation frequency [1], [2]. The oscillation may be quenched before reaching the nonlinear stage of the transient (linear operation) or after the nonlinear stage or the saturated amplitude is reached (nonlinear operation) [2], [13]. On the other hand, depending on the frequency of the quench signal, one may have a frozen or nonfrozen behavior [14], [15]. In the first case, obtained for the lower quench-signal frequencies, the system response is independent of this quench frequency, i.e., when normalizing the time to the quench-signal period, one obtains identical waveforms. In the second (nonfrozen) case, the response exhibits qualitative differences depending on the quench frequency. As a limit case, from a certain value of the quench-signal period, the oscillation will not have time to reach a significant amplitude before it is quenched again. As gathered from the above descriptions, the compactness of SROs comes at the expense of a complex operation, which, in addition to the timescale of the oscillation, involves the timescale of the quench signal.

In most previous works, the oscillator is modeled in a simplified manner with an *RLC* resonator and a single nonlinear element, often a cubic nonlinearity. This kind of model has enabled the thorough investigations of the SRO operation modes presented in the seminal works [2], [13]. However, in most cases, it will not enable a realistic prediction of the dynamics of transistor-based oscillators. To address this limitation, Hernández and Suarez [16], which focuses on SROs in linear mode, present a black-box model applicable to circuits with arbitrary topologies. It is based on the extraction of a linear-time-variant (LTV) transfer function from circuit-level envelope-transient simulations [17], [18]. This function is extracted (under a given quench signal) by considering a small-signal input whose frequency is varied in a certain band about the oscillation frequency. This is done by performing an envelope transient simulation at each frequency step. An integral expression [14], [16], based on the extracted LTV transfer function, provides the SRO response to any arbitrarily modulated small-signal input. In [19], the model was extended to the nonlinear operation mode by making use of the time-variant single-kernel [20] Volterra model of the SRO in the envelope domain. The resulting nonlinear

model was only applicable under certain constraints in the modulation of the input signal. In addition, a fundamental limitation of both the linear and nonlinear LTV models comes from the fact that they are derived for a particular quench signal; thus, they should be re-extracted under any variation of this signal. To generalize the analysis, Sancho et al. [21] propose a compact semianalytical formulation in the envelope domain, which is based on an outer tier description of the system at the oscillation frequency. It describes the system in both linear and nonlinear operations, and its parameters are obtained only once, from a single harmonic balance (HB). This is because the RF signal and the quench signal are taken as inputs of the formulation. Thus, unlike the black-box models in [16] and [19], this formulation is valid under any quench signal. However, the formulation in [21] suffers from an incomplete description of dynamic effects since the reduced-order envelope-domain formulation is written at the oscillation frequency only, disregarding the impact of the oscillator circuitry at the quench-signal frequency.

In this work, we present a two-band outer tier model of SROs in the envelope domain, which accounts for the oscillator circuitry at the oscillation band and at the quench-signal band. Its elements are easily extracted from HB by making use of two independent excitations in the two different bands. As will be shown, the new formulation provides useful insight into the switched oscillator behavior. This is because it enables the identification of the baseband component that determines the oscillator stability properties under the variation of the quench frequency. When increasing the quench frequency, this baseband component becomes attenuated and delayed with respect to the quench signal, which explains dynamic effects that cannot be predicted with previous models [21]. The model can be used for a system-level description of the SRO since it can efficiently predict its response under arbitrary input modulations and choices of the frequency and shape of the quench signal. The developed model will be validated through its application to an SRO at 2.8 GHz, which has been manufactured and experimentally characterized.

This article is organized as follows. Section II presents the new two-band model in the envelope domain, together with the procedure for the extraction of the model functions. Section III describes the application of the model to a FET-based SRO, considering different kinds of quench signals. Finally, Section IV presents the experimental results.

II. Two-Band Model in the Envelope Domain

A conceptual schematic of the SRO with its key signals is presented in Fig. 1. It is based on a suitably designed oscillator that, at a (representative) bias voltage V_q, oscillates at the frequency f_o. For the SRO operation, this bias voltage is replaced by a quench voltage source $v_q(t)$ [2], which will switch the oscillation on and off. The signal to be amplified is the RF input at a carrier frequency f_p, close to the oscillation frequency. In the "on" intervals of the quench signal, the oscillation grows from an initial condition that depends on the RF signal; as soon as $v_q(t)$ gets into the off interval, the oscillation decays, which gives rise to an output signal with a pulsed envelope (Fig. 1). In the following, we will derive a formulation considering both the baseband and the oscillation band; it will depart from the circuit-level HB formulation that describes the oscillator under a dc bias voltage. The formulation will be derived by first applying the implicit function theorem [22] and then introducing a slow timescale that will account for the effect of the quench signal and possible modulations. The procedure to extract the model parameters from standard HB simulations will also be described.

A. Static Two-Band Model

We will initially formulate the circuit in static conditions, i.e., with the quench voltage set to a dc value $v_q = V_q \in \Lambda_q$, where Λ_q is the voltage interval covered by $v_q(t)$ during the SRO operation. In single-tone HB, the circuit state variables $x(t) = (x_1, \ldots, x_d)^t \in R^d$ are expressed in a periodic Fourier basis with fundamental frequency $\omega_p = 2\pi f_p$. Applying the modified nodal approach [22], [23], [24], the HB system is derived by equating to zero the total current flowing into each node

$$F(X) + D(\omega_p)Q(X) + H(\omega_p)X + E = 0 \tag{1}$$

where the vectors X, F, Q, and E contain the harmonic components of the circuit state variables, the sums of resistive currents (that enter each node) and loop voltages, the linear and nonlinear charges and fluxes of the circuit, and the input generators, respectively. The vector E will contain the input signal and the bias voltages, including V_q. On the other hand, the diagonal matrix $D(\omega_p)$ multiplies by $jk\omega_p$ each kth harmonic component in Q, and the matrix $H(\omega_p)$ contains transfer functions associated with the distributed elements.

In the following, we will obtain an outer tier formulation with two observation nodes, one for the baseband and the other for the oscillation band, which may be defined at different circuit locations. To derive this formulation, we will consider the schematic in Fig. 2, in which the circuit is divided into a linear network and a nonlinear network. The quench signal is placed at the input of the linear network, whereas the output node of this network is directly connected to one of the terminals of the active device(s). This transistor terminal, with voltage $v_T(t)$, will constitute the baseband observation node. From this node, the currents entering the linear and nonlinear networks are called $i_L(t)$ and $i_T(t)$, respectively. The nonlinear network contains all the rest of the nonlinear and linear elements, including the output passive linear circuitry. The observation node at the oscillation band is defined at the output of the nonlinear network. It agrees with the one where the SRO output signal is obtained, with the voltage $v_{out}(t)$. The current $i_{out}(t)$ entering this node will also be considered in the formulation. Finally, the RF input source $v_{RF}(t) = V_p\cos(\omega_p t + \varphi)$ maybe included indistinctly in the linear or nonlinear network.

The two-band formulation will be derived from the application of Kirchhoff's current law (KCL) at dc and the fundamental frequency at the baseband and oscillation-band observation nodes, respectively. As will be demonstrated, this system reduction is enabled by the implicit function theorem [22]. The system, composed of the dc and

fundamental-frequency equations, included in system (1), is

$$\begin{aligned} I_0^{\mathrm{T}}\big(X,\omega_{\mathrm{p}}\big)+I_0^{\mathrm{L}}&=0\\ I_1^{\mathrm{out}}\big(X,\omega_{\mathrm{p}}\big)&=0 \end{aligned} \tag{2}$$

where I_0^{L}, I_0^{T}, and I_1^{out} are, respectively, the dc components of the periodic currents $i_{\mathrm{L}}(t)$ and $i_{\mathrm{T}}(t)$, and the fundamental-frequency component of $i_{\mathrm{out}}(t)$, as indicated by the subscripts. In general, subsystem (2) depends on all the harmonic components X of the circuit state variables through the current components I_0^{T} and I_1^{out}, which behave as nonlinear current functions. In the following, we will use the notation $\tilde{f}(\omega)\equiv F\{f(t)\}$ for the frequency-domain expression of any vector signal $f(t)$, where the operator F represents the Fourier transform. Then, the admittance matrix of the linear network in Fig. 2 provides the following frequency-domain expression of the current $i_{\mathrm{L}}(t)$ at the baseband:

$$\tilde{i}_{\mathrm{L}}(\omega)=\tilde{Y}_{\mathrm{L}1}(\omega)\tilde{v}_{\mathrm{T}}(\omega)+\tilde{Y}_{\mathrm{L}2}(\omega)\tilde{v}_{\mathrm{q}}(\omega) \tag{3}$$

where $|\omega|<\omega_{\mathrm{p}}/2$. The components $\tilde{Y}_{\mathrm{L}i}(\omega)$ can be easily identified through a linear simulation of the linear network since they are the elements of one of the rows of its 2×2 admittance matrix (see Fig. 2). Equation (3) can be combined with (2) to obtain

$$\begin{aligned} I_0^{\mathrm{T}}\big(X,\omega_{\mathrm{p}}\big)+\tilde{Y}_{\mathrm{L}1}(0)V_0+\tilde{Y}_{\mathrm{L}2}(0)V_{\mathrm{q}}&=0\\ I_1^{\mathrm{out}}\big(X,\omega_{\mathrm{p}}\big)&=0 \end{aligned} \tag{4}$$

where V_0 is the dc component of $v_{\mathrm{in}}(t)$. Using (1), and according to the implicit function theorem [22], one can state the dependence $X=X(V_0,V_1,\phi,V_{\mathrm{p}},\varphi,\omega_{\mathrm{p}})$, where V_1, ϕ and V_{p}, φ are the amplitudes and phases of the first harmonic components of $v_{\mathrm{out}}(t)$ and $v_{\mathrm{RF}}(t)$, respectively. Considering the above dependence, (4) becomes the following outer tier system:

$$\begin{aligned} I_0^{\mathrm{T}}\big(V_0,V_1,V_{\mathrm{p}},\varphi-\phi,\omega_{\mathrm{p}}\big)+\tilde{Y}_{\mathrm{L}1}(0)V_0+\tilde{Y}_{\mathrm{L}2}(0)V_{\mathrm{q}}&=0\\ I_1^{\mathrm{out}}\big(V_0,V_1,V_{\mathrm{p}},\varphi-\phi,\omega_{\mathrm{p}}\big)&=0 \end{aligned} \tag{5}$$

where the phase dependence of the functions I_0^{T} and I_1^{out} has the form $\varphi-\phi$. This is because, due to the oscillator autonomy, the whole system must be invariant under any constant time shift τ, which produces $(\varphi,\phi)\rightarrow\big(\varphi+\omega_{\mathrm{p}}\tau,\phi+\omega_{\mathrm{p}}\tau\big)$. The main interest of SROs lies in their capability to amplify signals of very small amplitude. Thus, we can assume that the RF amplitude V_{p} is small enough to approach the dependence on the RF input generator by the first-order Taylor series [25]

$$\begin{aligned} &I_0^{\mathrm{T}}\big(V_0,V_1,\omega_{\mathrm{p}}\big)+\tilde{Y}_{\mathrm{L}1}(0)V_0+\tilde{Y}_{\mathrm{L}2}(0)V_{\mathrm{q}}\\ &\quad+B_0^r V_{\mathrm{p}}\cos(\varphi-\phi)+V_{\mathrm{p}}B_0^i\sin(\varphi-\phi)=0\\ &I_1^{\mathrm{out}}\big(V_0,V_1,\omega_{\mathrm{p}}\big)+B_1^r V_{\mathrm{p}}\cos(\varphi-\phi)\\ &\quad+B_1^i V_{\mathrm{p}}\sin(\varphi-\phi)=0 \end{aligned} \tag{6}$$

where

$$\begin{aligned} B_0^{r,i}(V_0,V_1)&=\left.\frac{\partial I_0^{\mathrm{T}}\big(V_0,V_1,V_{\mathrm{p}},\varphi-\phi,\omega_{\mathrm{p}}\big)}{\partial U^{r,i}}\right|_{V_{\mathrm{p}}=0}\\ B_1^{r,i}(V_0,V_1)&=\left.\frac{\partial I_1^{\mathrm{out}}\big(V_0,V_1,V_{\mathrm{p}},\varphi-\phi,\omega_{\mathrm{p}}\big)}{\partial U^{r,i}}\right|_{V_{\mathrm{p}}=0} \end{aligned} \tag{7}$$

where $U^r=V_{\mathrm{p}}\cos\varphi$ and $U^i=V_{\mathrm{p}}\sin\varphi$. Note that the above first-order Tailor-series expansion will not prevent the prediction of a possible nonlinear response versus V_{p} since (6) exhibits nonlinear dependences on the other two variables V_0 and V_1. Now, introducing the baseband conductance function $G\equiv I_0^{\mathrm{T}}/V_0$ and the first harmonic admittance function $Y(V_0,V_1,\omega)$, system (6) can be rewritten as

$$\begin{aligned} &G\big(V_0,V_1,\omega_{\mathrm{p}}\big)V_0+\tilde{Y}_{\mathrm{L}1}(0)V_0+\tilde{Y}_{\mathrm{L}2}(0)V_{\mathrm{q}}\\ &\quad+B_0^r V_{\mathrm{p}}\cos(\varphi-\phi)+B_0^i V_{\mathrm{p}}\sin(\varphi-\phi)=0\\ &Y\big(V_0,V_1,\omega_{\mathrm{p}}\big)V_1+B_1^r V_{\mathrm{p}}\cos(\varphi-\phi)\\ &\quad+B_1^i V_{\mathrm{p}}\sin(\varphi-\phi)=0. \end{aligned} \tag{8}$$

System (8) constitutes a reduced-order description of the oscillator under a dc quench signal $V_{\mathrm{q}}\in\Lambda_{\mathrm{q}}$. In Section II-B, we will consider a time-varying quench signal $v_{\mathrm{q}}(t)$ as well as possible input-signal modulations $V_{\mathrm{p}}(t)$ and $\varphi(t)$.

B. Envelope-Domain Two-Band Model

Under a time-varying quench signal $v_{\mathrm{q}}(t)$, as well as the possible modulations $V_{\mathrm{p}}(t)$ and $\varphi(t)$, the baseband component becomes $V_0(t)$, whereas the component at the oscillation band becomes $V_1(t)e^{j\phi(t)}$. To predict the dynamics of these variables, we can set $\omega_{\mathrm{p}}\rightarrow\omega_{\mathrm{p}}+p$ in (8), where $p\equiv -js$ and s acts on the time-varying harmonics as a time-derivative operator [26]. The effect of this operator will be treated in a different manner in the two equations, at the baseband and at the oscillation frequency, respectively.

We will initially address the baseband equation of (8). Introducing p in this equation, one obtains

$$\begin{aligned} &G\big(V_0,V_1,\omega_{\mathrm{p}}\big)V_0(t)+\tilde{Y}_{\mathrm{L}1}(p)V_0(t)+\tilde{Y}_{\mathrm{L}2}(p)v_{\mathrm{q}}(t)\\ &\quad+B_0^r V_{\mathrm{p}}\cos(\varphi-\phi)+B_0^i V_{\mathrm{p}}\sin(\varphi-\phi)=0 \end{aligned} \tag{9}$$

where the dependence of G on p has been neglected since its impact is very small in comparison with that of the terms $\tilde{Y}_{\mathrm{L}1}(p)$ and $\tilde{Y}_{\mathrm{L}2}(p)$, which accounts for the baseband circuitry through which the quench signal is introduced. In an integral form, (9) is expressed as

$$\begin{aligned} &G\big(V_0,V_1,\omega_{\mathrm{p}}\big)V_0(t)+Y_{\mathrm{L}1}*V_0(t)+Y_{\mathrm{L}2}*v_{\mathrm{q}}(t)\\ &\quad+B_0^r(V_0,V_1)V_{\mathrm{p}}\cos(\varphi-\phi)\\ &\quad+B_0^i(V_0,V_1)V_{\mathrm{p}}\sin(\varphi-\phi)=0 \end{aligned} \tag{10}$$

where the operator $*$ means convolution and, following the notation used in this article, $Y_{\mathrm{L}1}(t)=\mathcal{F}^{-1}\big\{\tilde{Y}_{\mathrm{L}1}(\omega)\big\}$ and $Y_{\mathrm{L}2}(t)=\mathcal{F}^{-1}\big\{\tilde{Y}_{\mathrm{L}2}(\omega)\big\}$. Because the amplitude and phase modulation of the RF signal are slow, we have neglected the time derivatives of $V_{\mathrm{p}}(t)$ and $\varphi(t)$.

Now, we will address the equation of (8) at the oscillation band. The admittance function $Y\big(V_0,V_1,\omega_{\mathrm{p}}\big)$ in (8) is modified by setting $\omega_{\mathrm{p}}\rightarrow\omega_{\mathrm{p}}+p$, which provides [22]

$$\begin{aligned} &Y\big(V_0,V_1,\omega_{\mathrm{p}}-js\big)V_1e^{j\phi}\\ &\quad\simeq Y\big(V_0,V_1,\omega_{\mathrm{p}}\big)V_1e^{j\phi}\\ &\quad\quad-jY_{\omega}\big(V_0,V_1,\omega_{\mathrm{p}}\big)\big(\dot{V}_1+jV_1\dot{\phi}\big)e^{j\phi}. \end{aligned} \tag{11}$$

As in most piecewise circuit-level envelope domain formulations [17], [27], we have developed Y in a first-order

Taylor series, using $Y_\omega \equiv \partial Y/\partial\omega$ [22]. Using (11), the oscillation-band equation in (8) becomes

$$\begin{aligned} Y\left(V_0, V_1, \omega_\mathrm{p}\right)V_1 - jY_\omega\left(V_0, V_1, \omega_\mathrm{p}\right)\left(\dot{V}_1 + jV_1\dot{\phi}\right) \\ + B_1^r(V_0, V_1)V_\mathrm{p}\cos(\varphi-\phi) \\ + B_1^i(V_0, V_1)V_\mathrm{p}\sin(\varphi-\phi) = 0. \end{aligned} \tag{12}$$

The nonlinear system composed by (10) and (12) describes the SRO dynamics using the state variables (V_0, V_1, ϕ). Because of the dependence on the oscillation amplitude V_1, the above system can describe the SRO dynamics both in linear and logarithmic modes. It can be solved by discretizing the convolution operations of the baseband equation and applying any explicit or implicit integration method, like Runge–Kutta or backward-Euler. Note that this formulation has the advantage of providing a compact reduced-order model of the SRO; because the observation node corresponds to that of the output signal, $v_\mathrm{out}(t)$, it can be easily incorporated as an input–output black box of a given system. Because it is derived from an HB formulation, it will not suffer from any of the uncertainties or convergence problems that could be encountered in the (more complex) circuit-level envelope domain. The model involves a set of nonlinear complex functions $\left(G, Y, Y_\omega, B_0^r, B_0^i, B_1^r, B_1^i\right)$, which are calculated using circuit-level HB, as described in Section II-C.

C. Identification of the Nonlinear Functions of the Two-Band System

In the first step, we will calculate the functions G, Y, and Y_ω in circuit-level HB. They will be obtained for a given ω_p through the following procedure, illustrated in Fig. 3. Both the quench source and the input RF source are short-circuited ($v_\mathrm{q} = v_\mathrm{RF} = 0$). Then, we introduce two auxiliary sources: 1) an auxiliary dc voltage source V_0, playing the role of the dc voltage variable V_0 in (10)–(12). It is connected at the baseband observation node in series with a dc feed and 2) an auxiliary generator (AG), playing the role of the voltage variable V_1 in (10)–(12). It is connected at the oscillation observation node. This AG is composed of a one-tone voltage source of amplitude V_1, phase 0, and frequency ω_AG in series with an ideal filter of admittance $Y_\mathrm{f}(\omega) = \delta(\omega - \omega_\mathrm{AG})$. In the presence of the auxiliary sources, the values of (V_0, V_1) are fixed by the amplitudes of these sources and the circuit fulfills

$$\begin{aligned} \left(\tilde{Y}_{\mathrm{L1}}(0) + G(V_0, V_1, \omega_\mathrm{AG})\right)V_0 &= I_\mathrm{dc}(V_0, V_1, \omega_\mathrm{AG}) \\ Y(V_0, V_1, \omega_\mathrm{AG})V_1 &= I_\mathrm{AG}(V_0, V_1, \omega_\mathrm{AG}) \end{aligned} \tag{13}$$

where I_dc is the current through the dc voltage source V_0 and I_AG is the current through the voltage source V_1. The current functions $I_\mathrm{dc}(V_0, V_1, \omega_\mathrm{AG})$ and $I_\mathrm{AG}(V_0, V_1, \omega_\mathrm{AG})$ can be calculated by solving the circuit of Fig. 3 in circuit-level HB. Once these functions are available, the nonlinear coefficients in (10) and (11) are deduced from (13) as

$$G\left(V_0, V_1, \omega_\mathrm{p}\right) = \frac{I_\mathrm{dc}\left(V_0, V_1, \omega_\mathrm{p}\right)}{V_0} - \tilde{Y}_{\mathrm{L1}}(0) \tag{a}$$

$$Y\left(V_0, V_1, \omega_\mathrm{p}\right) = \frac{I_\mathrm{AG}\left(V_0, V_1, \omega_\mathrm{p}\right)}{V_1} \tag{b}$$

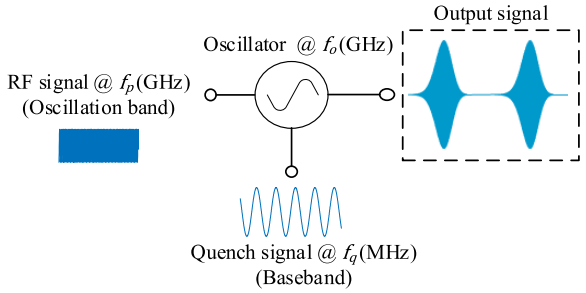

Fig. 1. SRO schematic showing the two different frequency bands involved in its operation.

$$Y_\omega\left(V_0, V_1, \omega_\mathrm{p}\right) \simeq \frac{1}{V_1}\frac{I_\mathrm{AG}\left(V_0, V_1, \omega_\mathrm{p}+d\omega\right) - I_\mathrm{AG}\left(V_0, V_1, \omega_\mathrm{p}\right)}{d\omega}. \tag{c}$$

(14)

Note that, in order to estimate Y_ω at each point (V_0, V_1),the current function I_AG must be calculated for $\omega_\mathrm{AG} = \omega_\mathrm{p}, \omega_\mathrm{p} + d\omega$, where $d\omega$ is a frequency shift small enough to allow the accurate application of the method of finite differences. The three numerical functions in (14) are obtained through a double sweep in (V_0, V_1).

In the second step, we will calculate the functions B_0^r, B_0^i, B_1^r, and B_1^i. We will use the same implementation of Fig. 3 and introduce a small-signal RF input source: $v_\mathrm{RF}(t) = \varepsilon\cos\left(\omega_\mathrm{p}t + \varphi\right)$. In the first analysis, to calculate the nonlinear coefficients $B_0^r(V_0, V_1)$ and $B_1^r(V_0, V_1)$, the phase of the RF signal is set to $\varphi = 0$, corresponding to $U^r = \varepsilon$ and $U^i = 0$ in (7). Then, these functions are given by

$$\begin{aligned} B_0^r(V_0, V_1) &\simeq \frac{I_\mathrm{dc}\left(V_0, V_1, \omega_\mathrm{p}, \varepsilon\right) - I_\mathrm{dc}\left(V_0, V_1, \omega_\mathrm{p}, 0\right)}{\varepsilon} \\ B_1^r(V_0, V_1) &\simeq \frac{I_\mathrm{AG}\left(V_0, V_1, \omega_\mathrm{p}, \varepsilon\right) - I_\mathrm{AG}\left(V_0, V_1, \omega_\mathrm{p}, 0\right)}{\varepsilon} \end{aligned} \tag{15}$$

where $I_\mathrm{dc}\left(V_0, V_1, \omega_\mathrm{p}, 0\right)$ and $I_\mathrm{AG}\left(V_0, V_1, \omega_\mathrm{p}, 0\right)$ are the current functions for $v_\mathrm{RF} = 0$. In turn, the nonlinear coefficients $B_0^i(V_0, V_1)$ and $B_1^i(V_0, V_1)$ are calculated using this same procedure but setting the phase of the RF signal to $\varphi = \pi/2$, which corresponds to $U^r = 0$ and $U^i = \varepsilon$ in (7).

Once the nonlinear functions are available, the system composed by (10) and (12) is ready to be integrated. To clarify the accuracy improvements, in Section II-D, the new formulation will be analytically compared with the previous single-band formulation, presented in [21]. In Section III, the two formulations will be numerically compared through their application to a FET-based SRO in Section III.

D. Comparison With the Single-Band Formulation in [21]

In the single-band formulation of the previous work [21], the SRO dynamics is determined by the following equation at the oscillation band:

$$Y_\mathrm{s}\left(v_\mathrm{q}, V_1, \omega_\mathrm{p}\right)V_1 e^{j\phi} - jY_{s\omega}\left(v_\mathrm{q}, V_1, \omega_\mathrm{p}\right)\left(\dot{V}_1 + jV_1\dot{\phi}\right)e^{j\phi} = I_\mathrm{p}e^{j\varphi} \tag{16}$$

where $I_\mathrm{p}e^{j\varphi}$ is the Norton equivalent of the RF source at the observation node and the nonlinear admittance function $Y_\mathrm{s}\left(v_\mathrm{q}, V_1, \omega_\mathrm{p}\right)$ depends directly on v_q. Thus, in [21], there is

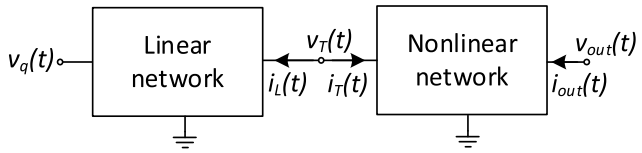

Fig. 2. Schematic of the SRO used for the development of the two-band formulation. The circuit is divided into a linear and a nonlinear network.

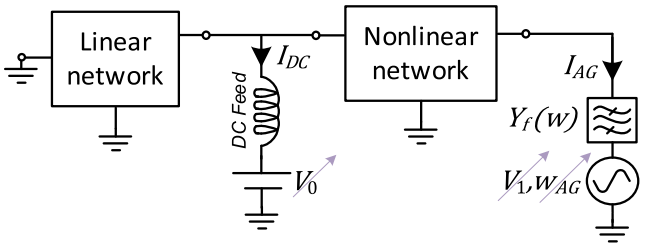

Fig. 3. Schematic used to extract the nonlinear functions required by the new formulation from circuit-level HB. For the calculation of (G, Y, Y_ω), the quench and RF input generators are disabled $(v_q = v_{RF} = 0)$. The functions (G, Y) are calculated for $\omega_{AG} = \omega_p$, whereas the function Y_ω is calculated by using the HB results for $\omega_{AG} = \omega_p$ and $\omega_{AG} = \omega_p + d\omega$. For the calculation of $\left(B_0^r, B_0^i, B_1^r, B_1^i\right)$, the quench and RF input generators are $v_q = 0$ and $v_{RF}(t) = \varepsilon\cos(\omega_p t + \varphi)$, and the AG frequency is fixed to $\omega_{AG} = \omega_p$. The functions $\left(B_0^r, B_1^r\right)$ are calculated by setting $\varphi = 0$, whereas the functions $\left(B_0^i, B_1^i\right)$ are calculated by setting $\varphi = \pi/2$.

no explicit dependence on the state variable V_0. Instead, that dependence is implicit through the HB system (1). In this HB system, the equation relating V_0 with the bias voltage V_q can be expressed using the networks introduced in Fig. 2 as [see (4)]

$$I_0^T + \tilde{Y}_{L1}(0)V_0 + \tilde{Y}_{L2}(0)V_q = 0. \tag{17}$$

Because (17) is a dc equation, there is no frequency dependence in $\tilde{Y}_{L1}(0)$ and $\tilde{Y}_{L2}(0)$. In (16), this dc equation remains implicit in the HB system, unlike the case of the new formulation. As a result, the dynamic effects resulting from the frequency dependence of $\tilde{Y}_{L1}(\omega)$ and $\tilde{Y}_{L2}(\omega)$ are ignored since (16) cannot account for them. In contrast, the two-band formulation overcomes this problem by explicitly considering the baseband KCL equation that relates V_0 and V_q in the static system (4). When producing the dynamic system (10), the time-varying functions $Y_{L1}(t)$ and $Y_{L2}(t)$, accounting for the baseband dynamics, are obtained from $\tilde{Y}_{L1}(\omega)$ and $\tilde{Y}_{L2}(\omega)$.

To get analytical insight, we will compare the initial (linear) startup transient predicted by the two formulations. In the two cases, we will consider a time-varying quench source $v_q(t)$, as well as $v_{RF} = 0$, for simplicity. With the new formulation, the startup equation can be derived by splitting (12) into real and imaginary parts and solving for $\dot{V}_1$. Near $V_1 = 0$(initial (linear) startup transient), this provides the following phase-independent equation, governing the amplitude dynamics:

$$\begin{aligned}\dot{V}_1 &= -\frac{Y\left(V_0, 0, \omega_p\right) \cdot Y_\omega\left(V_0, 0, \omega_p\right)}{\left|Y_\omega\left(V_0, 0, \omega_p\right)\right|^2} V_1 \\ &= \sigma(V_0) V_1\end{aligned} \tag{18}$$

where the operator $\cdot$ is defined as $a \cdot b = \mathrm{Re}(a)\mathrm{Re}(b) + \mathrm{Im}(a)\mathrm{Im}(b)$. Thus, the stability of the solution $V_1 = 0$ is determined by the pole $\sigma(V_0)$, so the oscillation startup condition is $\sigma(V_0) > 0$. Equation (18) can be compared with the one derived from (16) and given by [21]

$$\begin{aligned}\dot{V}_1 &= -\frac{Y_s\left(v_q, 0, \omega_p\right) \cdot Y_{s\omega}\left(v_q, 0, \omega_p\right)}{\left|Y_{s\omega}\left(v_q, 0, \omega_p\right)\right|^2} V_1 \\ &= \alpha\left(v_q\right) V_1.\end{aligned} \tag{19}$$

There is a significant difference between the two equations. The pole in (18) depends on V_0, whereas the pole in (19), given by $\alpha\left(v_q\right)$, directly depends on v_q. The value of these two poles will agree if the quench voltage is set to a dc value $v_q = V_q$ since the two formulations are consistent with the HB system (1). However, the quench signal is time-variant $\left(v_q = v_q(t)\right)$ so one should numerically integrate the corresponding differential equations. Then, for low values of the quench frequency f_q, we will have $\alpha\left(v_q(t)\right) \simeq \sigma(V_0(t))$, $\forall t$, since for low frequencies $\tilde{Y}_{L1}(\omega) \simeq \tilde{Y}_{L1}(0)$, $\tilde{Y}_{L2}(\omega) \simeq \tilde{Y}_{L2}(0)$. However, as f_q increases, the frequency dependence of $\tilde{Y}_{L1}(\omega)$ and $\tilde{Y}_{L2}(\omega)$ will become relevant, so $\alpha\left(v_q(t)\right) \neq \sigma(V_0(t))$. As a result, the startup transient predicted with the two formulations will be different.

Note that we have considered the case of the initial (linear) startup transient because it is analytically tractable and provides insight into the differences between the two formulations. The general dependences in the full SRO operation are more complex and cannot be expressed in an analytical manner. Thus, the prediction capabilities of the two formulations will be numerically compared through their application to a FET-based SRO.

III. Application to a FET-Based SRO

The FET-based SRO, shown in Fig. 4, makes use of an ATF-34143 HEMT with series feedback. Ideal models will be considered for the lumped components, i.e., capacitors, inductors, and resistors, whereas the transmission lines will be modeled using the physical dimensions and parameters of the substrate (Rogers RO4003C, $h = 32$ mil, and $\varepsilon_r = 3.55$). The transistor model (ATF34143-PHEMT) used for all the simulations is the one provided by Avago Technologies (Broadcom Ltd., San Jose, CA, USA). This model includes the losses of the ceramic microstrip package (SOT-343). The SRO is intended to operate at 2.7 GHz. The circuit division into a linear and a nonlinear network (as shown in the sketch of Fig. 2) is explicitly indicated in Fig. 4. Note that the quench signal $v_q$undergoes a low-pass filtering due to the combined effect of the dc choke and the dc-block capacitor. The input RF source $v_{RF}(t)$ is placed inside the linear network, and $v_{out}(t)$ is the voltage signal that will be used to observe the oscillation dynamics.

Since the transistor is an n-channel depletion-mode device, at low frequencies, it provides high impedance at the gate terminal, yielding $I_0^T \simeq 0$ in (4). Therefore, in this particular case, the baseband equation (10) reduces to

$$\tilde{V}_0(\omega) \simeq H_L(\omega)\tilde{v}_q(\omega) \tag{20}$$

where $H_L(\omega) = -\tilde{Y}_{L2}(\omega)/\tilde{Y}_{L1}(\omega)$ and $H_L(0) = 1$. Initially, we have verified the capabilities of the formulation to predict the stability variations versus the voltage value V_0, which, as explained in Section II-A (and verified later), is the one

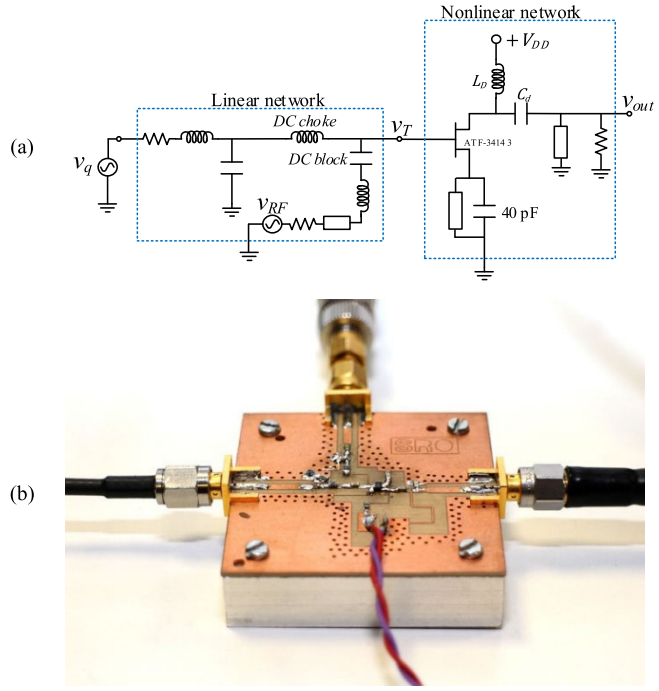

Fig. 4. FET-based SRO at 2.8 GHz based on the transistor ATF-34143 with series feedback: (a) schematic of the circuit, showing the division into a linear and a nonlinear network (as shown in the sketch of Fig. 2) and (b) photograph of the circuit.

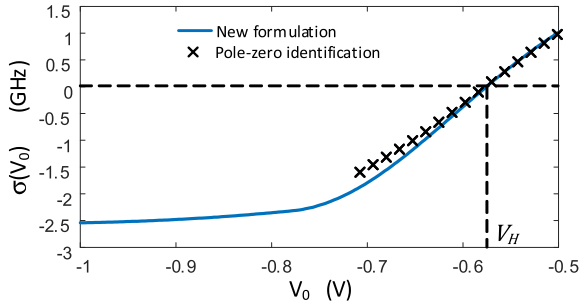

Fig. 5. Small-signal stability analysis. The pole $\sigma(V_0)$ indicates that the oscillation startup takes place for the gate bias value $V_0 = V_H = -0.57$ V.

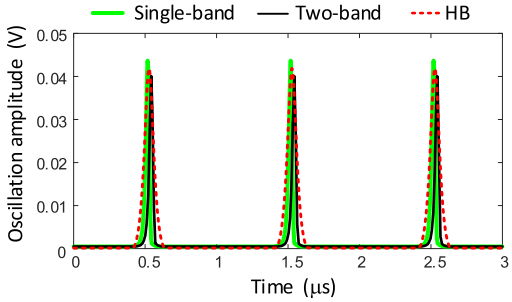

Fig. 6. SRO in linear mode. The amplitude at the fundamental frequency is represented versus time. The results of the single-band and two-band models are compared with those of the circuit-level envelope-transient simulation. The quench voltage is a sinusoidal signal $v_q(t) = B_q + A_q \cos 2\pi f_q t$, where $A_q = 0.71$ V, $B_q = -1.3$ V, $V_p = 0.5$ mV, and $f_q = 1$ MHz.

that determines the oscillation startup. Fig. 5 presents the pole function $\sigma(V_0)$ obtained from (18). This shows that the oscillation starts up for $V_0 > V_H = -0.57$ V. The results have been validated with a stability analysis at the circuit level based on pole–zero identification [15], [28]. This analysis has been carried out by setting the quench source to a dc value V_q and obtaining the value $V_0(V_q)$ and the input dc-impedance $Z(\omega, V_q)$ at a given circuit node. Then, the poles of the transfer function $Z(-js, V_q)$ are identified in IVCAD ©Maury Microwave for a sweep in V_q. The curve providing the real part of the pair of dominant complex-conjugate poles is overlapped with $\sigma(V_0)$in Fig. 5. Finally, note that, in dc operation, (20) produces $V_0 \simeq H_L(0)V_q = V_q$. Therefore, the oscillation startup condition in the single-band system can be expressed in terms of the gate bias voltage as $V_q > V_H$.

In the following, the new two-band formulation will be tested in two qualitatively different analyses: with a sinusoidal quench voltage source and with a rectangular one.

A. Sinusoidal Quench Voltage Source

Initially, we will address the SRO in the commonly used linear mode. It will be analyzed using both the two-band formulation [see (10) and (12)] and the single-band formulation (16), and the results will be compared with those provided by circuit-level envelope transient in commercial HB software. The sinusoidal quench voltage source is given by $v_q(t) = B_q + A_q \cos 2\pi f_q t$, with $A_q = 0.71$ V, $B_q = -1.3$ V, $V_p = 0.5$ mV, and $f_q = 1$ MHz. The results are shown in Fig. 6, where the oscillation amplitude $V_1(t)$ at the circuit output has been represented versus time. The slight discrepancies with circuit-level envelope transient are explained because the two-band model makes use in (11) of a first-order Taylor series of the admittance function Y in the ω variable. This kind of Taylor series expansion in terms of ω is of common use in circuit-level envelope transient based on a piecewise HB formulation [17], [27]. Thus, it is not peculiar to the SRO model derived here. The accuracy of the model could be improved by increasing the order of the series or the number of variables considered.

Next, we will analyze the dynamical effects. The sinusoidal quench voltage source is now given by $v_q(t) = B_q + A_q \cos 2\pi f_q t$, with $A_q = 0.9$ V and $B_q = -1.3$ V, and $V_p = 0.5$ mV. The results will be compared with those obtained with circuit-level envelope transient when using NH = 21 harmonic terms. Fig. 7(a) presents the time variation of the oscillation amplitude $V_1(t)$ at the circuit output, obtained through the three methods for $f_q = 1$ MHz. From the inspection of the waveform, which reaches the steady-state oscillation amplitude, the SRO is operating in nonlinear mode, which demonstrates the capability of the model to predict this regime. The signals $v_q(t)$ and $V_0(t)$ are compared in Fig. 7(b), which allows identifying the time values at which the oscillation is triggered. Remember that, as shown in Fig. 5, the formulation pole fulfills $\sigma(V_0) > 0$for $V_0 > V_H$. When $V_0(t) > V_H$, the oscillation is triggered, and the amplitude $V_1(t)$ grows toward the saturated value. Both the single-band and the two-band formulations present a good agreement with the circuit-level envelope-transient simulation. At this low frequency ($f_q = 1$ MHz), $\tilde{Y}_{Li}(\omega) \simeq \tilde{Y}_{Li}(0)$ for $i = 1, 2$ and therefore, $V_0(t) \simeq v_q(t)$ as in the dc operation mode. The improvement achieved with the new two-band formulation is better observed in the zoomed-in view of a single pulse, presented in Fig. 7(c). The

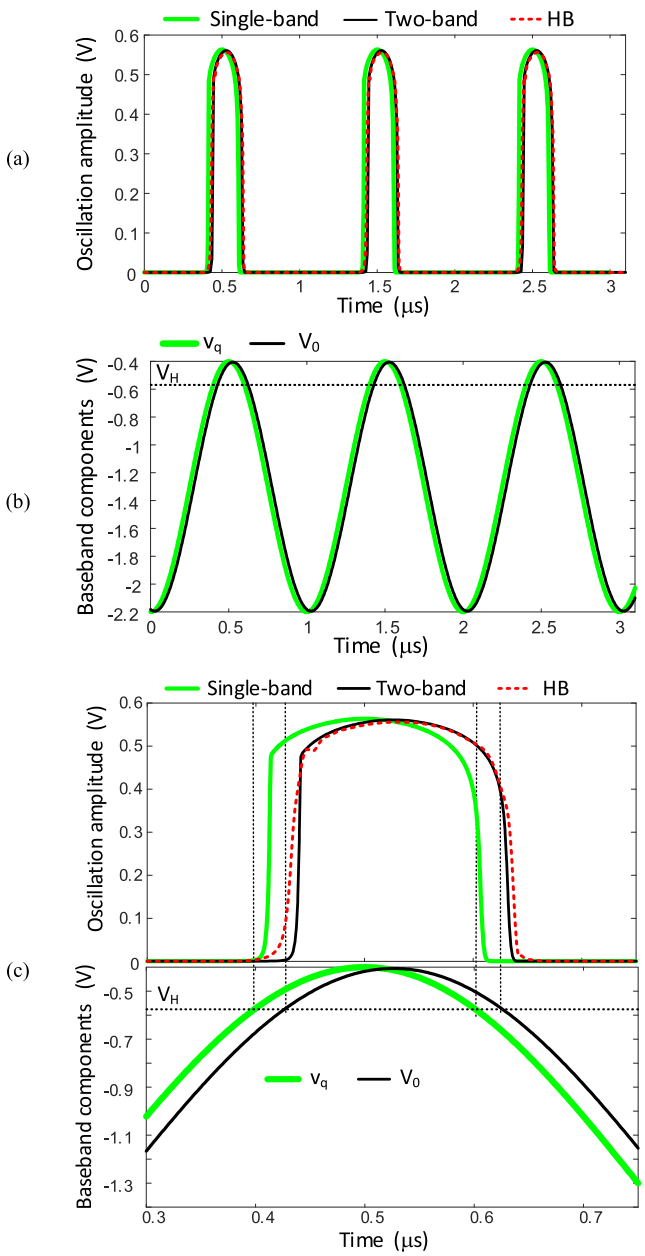

Fig. 7. Analysis of the SRO performance. The results of the single-band and two-band techniques are compared with those of the circuit-level envelope-transient simulation. The quench voltage is a sinusoidal signal $v_q(t) = B_q + A_q \cos 2\pi f_q t$, where $A_q = 0.9$ V, $B_q = -1.3$ V, $V_p = 0.5$ mV, and $f_q = 1$ MHz: (a) amplitude at the fundamental frequency $V_1(t)$; (b) baseband components $v_q(t)$ and $V_0(t)$; and (c) zoomed-in view of (a) and (b).

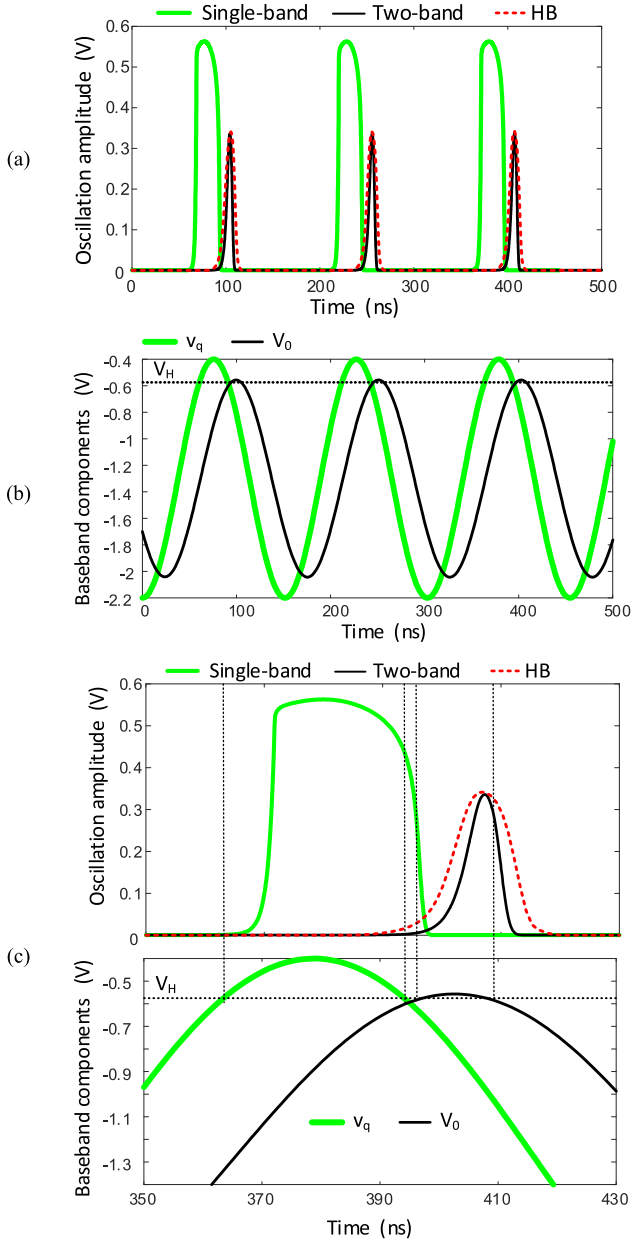

Fig. 8. Analysis of the SRO performance. The results of the single-band and two-band formulations are compared with those of circuit-level envelope-transient simulation. The quench voltage is a sinusoidal signal $v_q(t) = B_q + A_q \cos 2\pi f_q t$, where $A_q = 0.9$ V, $B_q = -1.3$ V, $V_p = 0.5$ mV, and $f_q = 6.6$ MHz: (a) amplitude at the fundamental frequency $V_1(t)$; (b) baseband components $v_q(t)$ and $V_0(t)$; and (c) zoomed-in views of (a) and (b).

signal $V_1(t)$ predicted by the single-band formulation (16) is time advanced with respect to the one simulated with both the two-band and the circuit-level simulation. This is consistent with the shift of the baseband voltage $V_0(t)$ with respect to $v_q(t)$ [Fig. 7(c)] because of the baseband components $\tilde{Y}_{L1}(\omega)$ and $\tilde{Y}_{L2}(\omega)$. As a result, the time interval for which the startup condition $V_0(t) > V_H$ is fulfilled is time-shifted with respect to $v_q(t) > V_H$. Remember that, as explained in Section II-C, in the single-band system (16), the oscillation startup is directly triggered by $v_q(t)$, missing the baseband effects produced by $\tilde{Y}_{L1}(\omega)$ and $\tilde{Y}_{L2}(\omega)$.

In Fig. 8, the quench frequency has been increased to $f_q = 6.6$MHz. As can be seen, the bias voltage $V_0(t)$ no longer agrees with $v_q(t)$. Indeed, it is attenuated and phase-shifted with respect to $v_q(t)$ by the effect of the baseband components $\tilde{Y}_{L1}(\omega)$ and $\tilde{Y}_{L2}(\omega)$. Consequently, the time interval for which the startup condition $V_0(t) > V_H$ is fulfilled is shorter and time-shifted with respect to $v_q(t) > V_H$, yielding a smaller growth of $V_1(t)$. The single-band formulation (16) is unable to predict this behavior, whereas the two-band formulation agrees with the circuit-level envelope-transient simulation.

Finally, if the quench frequency f_q is further increased, the oscillation is nearly annihilated, as shown in Fig. 9(a) for

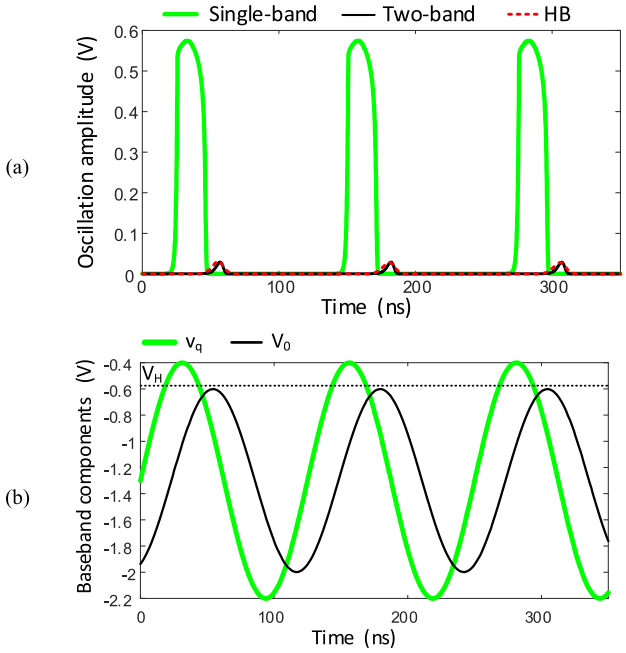

Fig. 9. Analysis of the SRO performance. The results of the single-band and two-band techniques are compared with those of the circuit-level envelope-transient simulation. The quench voltage is a sinusoidal signal $v_q(t) = B_q + A_q \cos 2\pi f_q t$, where $A_q = 0.9$ V, $B_q = -1.3$ V, $V_p = 0.5$ mV, and $f_q = 8$ MHz: (a) amplitude at the fundamental frequency $V_1(t)$ and (b) baseband components $v_q(t)$ and $V_0(t)$.

$f_q = 8$ MHz. This is because for this frequency value, the baseband component V_0 is attenuated below the threshold V_H [Fig. 9(b)]. Thus, the new formulation provides a condition valid for all values of the quench signal, regardless of the frozen or nonfrozen behavior. As can be seen, even though the oscillation condition $V_0 > V_H$ is not fulfilled anymore, the oscillation component $V_1(t)$ still shows a little bump, obtained when the baseband component $V_0(t)$ gets close to V_H; this is due to the amplification resulting from the low σ value. The effect is similar to that obtained in a reflection amplifier when its dominant complex-conjugate poles approach the imaginary axis [29].

B. Rectangular Quench Voltage Source

Now the case of a rectangular quench voltage source is considered, represented as a periodic pulse train

$$v_q(t) = B_q + A_q \sum_{k=-\infty}^{\infty} p\left(t - kT_q\right) \tag{21}$$

where

$$p(t) = \begin{cases} 1, & 0 \le t < T_q/2 \\ 0, & \text{otherwise} \end{cases} \tag{22}$$

and $T_q = 1/f_q$. As in the sinusoidal case, the values $A_q = 0.9$ V and $B_q = -1.3$ V have been chosen. Then, the voltage source ideally activates the oscillation during the upper part of the pulses ($v_q(t) = -0.4V > V_H$) and deactivates it during the lower part ($v_q(t) = -2.2$ V $< V_H$). The analysis has been carried out for the same quench frequencies of the sinusoidal case. The simulation results for $f_q = 1$ MHz are shown in

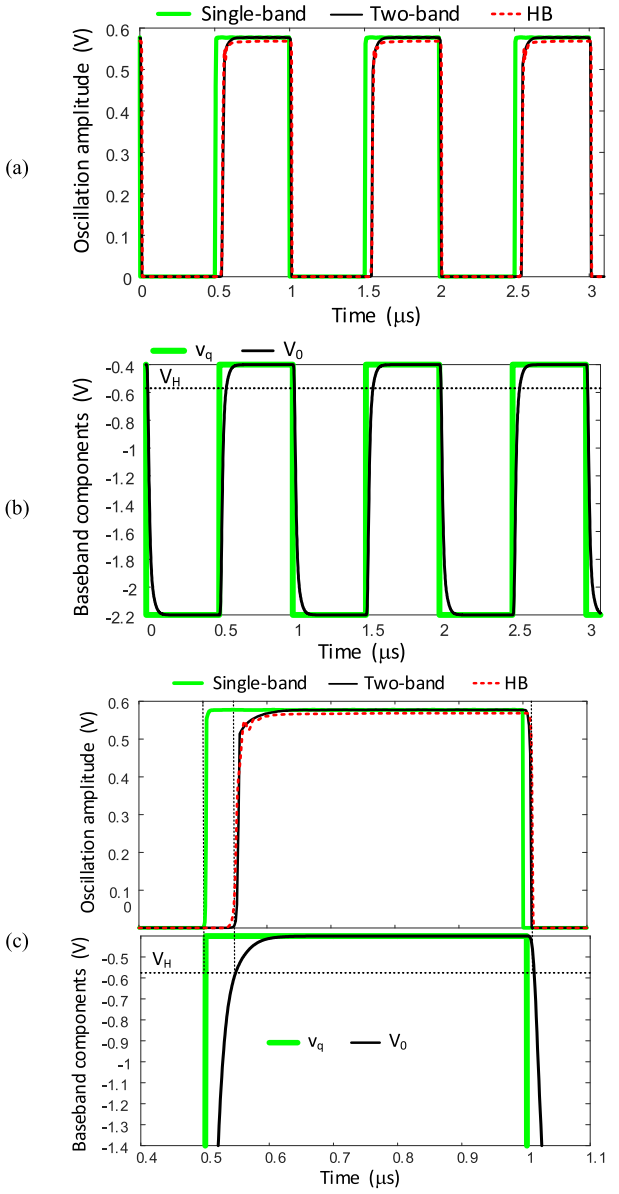

Fig. 10. Analysis of the SRO performance. The results of the single-band and two-band techniques are compared with those of the circuit-level envelope–transient simulation. The quench voltage is a periodic pulse train given by (21) where $A_q = 0.9$ V, $B_q = -1.3$ V, $V_p = 0.5$ mV, and $f_q = 1$ MHz: (a) amplitude at the fundamental frequency $V_1(t)$; (b) baseband components $v_q(t)$ and $V_0(t)$; and (c) zoomed-in views of (a) and (b).

Fig. 10. In the case of the single-band formulation, the oscillation is triggered by the quench signal $v_q(t)$. However, the signal $V_0(t)$ exhibits some differences with respect to $v_q(t)$[see Fig. 10(b) and the zoomed-in view in Fig. 10(c)], which explains the behavior of $V_1(t)$ obtained with both circuit-level envelope transient and the two-band formulation. On the one hand, $V_0(t)$is delayed with respect to $v_q(t)$, which gives rise to the delay in $V_1(t)$. On the other hand, $V_0(t)$ is smoothed in comparison with $v_q(t)$, which is due to the baseband network filtering effects. As a result, the growing transient is slower when simulated with the two-band formulation [which follows $V_0(t)$], in agreement with the circuit-level envelope-transient simulation [see Fig. 10(a) and (c)].

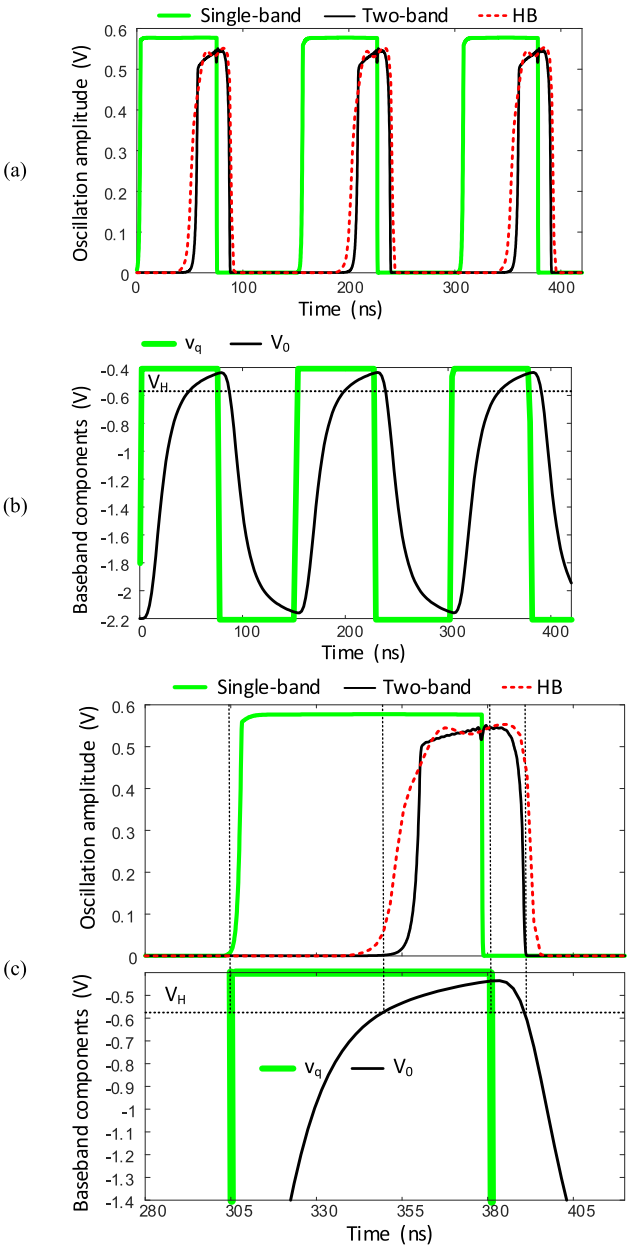

Fig. 11. Analysis of the SRO performance. The results of the single-band and two-band techniques are compared with those of the circuit-level envelope–transient simulation. The quench voltage is a periodic pulse train given by (21) where $A_q = 0.9$ V, $B_q = -1.3$ V, $V_p = 0.5$ mV, and $f_q = 6.6$ MHz: (a) amplitude at the fundamental frequency $V_1(t)$; (b) baseband components $v_q(t)$ and $V_0(t)$; and (c) zoomed-in views of (a) and (b).

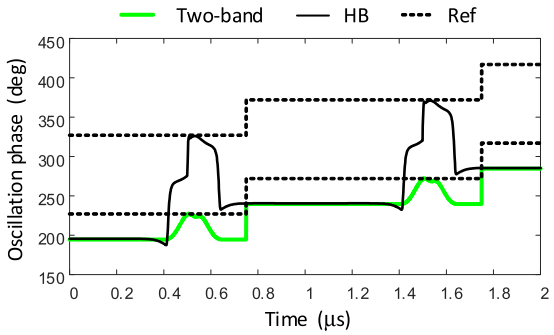

Fig. 12. Simulation of the first-harmonic phase variable $\phi(t)$. The quench voltage is a sinusoidal signal $v_q(t) = B_q + A_q \cos 2\pi f_q t$, where $A_q = 0.7$ V, $B_q = -1.3$ V, $V_p = 0.5$ mV, and $f_q = 1$ MHz. Comparison of the results of the two bands with those obtained with circuit-level envelope transient.

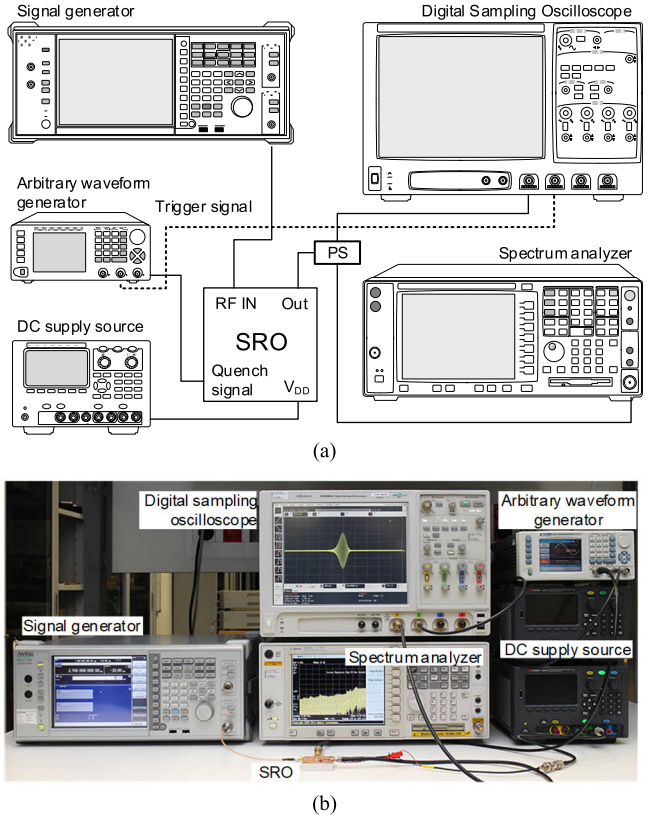

Fig. 13. Measurement setup including an Anritsu MG3710A VSG, providing the RF input to the SRO, and a WW2572A arbitrary waveform generator, providing the quench signal. The output of the SRO has been connected to a spectrum analyzer and a digital storage oscilloscope (DSO90804A): (a) schematic and (b) photograph.

Next, the quench frequency is set to $f_q = 6.6$ MHz, which provides the results in Fig. 11. In this case, the baseband filtering effects on $V_0(t)$ are more noticeable. This effect is transferred to the amplitude $V_1(t)$ when analyzed with both the two-band formulation and circuit-level envelope transient. Indeed, since $V_0(t)$ fulfills $V_0(t) > V_H$ for a shorter time than in the low-frequency case, the oscillating region gets narrower in the cycle, and the growing transient of $V_1(t)$ attains a lower amplitude. This phenomenon is not detected by the single-band formulation, which follows the startup condition $v_q(t) > V_H$, so the relative width of the oscillating region is similar to that of the low-frequency case. Note that the top of the pulses obtained with circuit-level envelope-transient simulation exhibits some ripple [Fig. 11(c)]. It is produced by the introduction of a multiharmonic signal in a nonlinear high-order system. This behavior is partially reproduced by the two-band formulation, due to the order reduction of the systems (10) and (11) in comparison with circuit-level envelope-transient.

So far, we have analyzed the effect of the quench-signal frequency on the amplitude of the output pulses. It will also be interesting to analyze the output phase. However, due to the unlocked operation of the SRO, there is an invariance

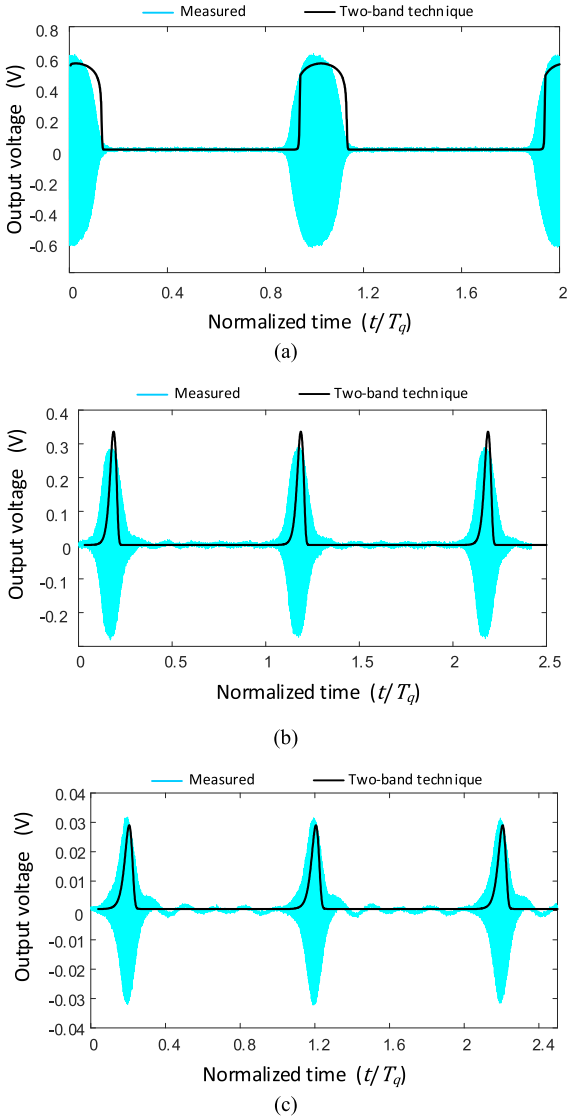

Fig. 14. Measured SRO performance, with simulations superimposed. The quench voltage is a T_q- periodic sinusoidal signal $v_q(t) = B_q + A_q \cos 2\pi f_q t$, where $A_q = 0.9$ V, $B_q = -1.3$ V, and $T_q = 1/f_q$: (a) $f_q = 2$ MHz; (b) $f_q = 5$ MHz; and (c) $f_q = 6$ MHz.

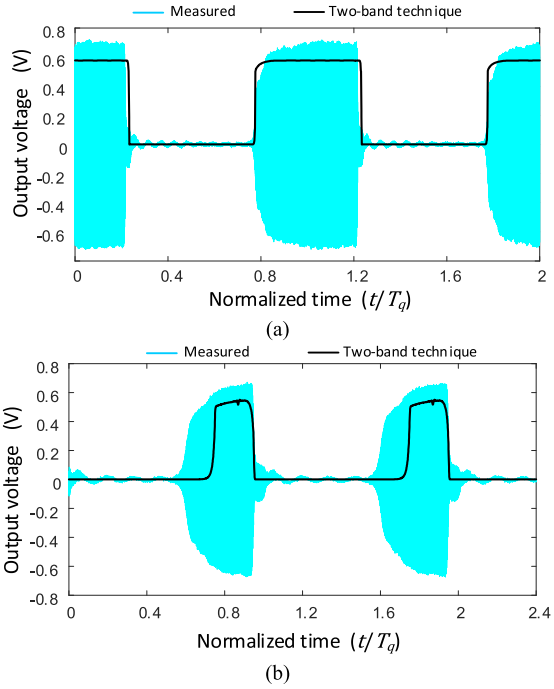

Fig. 15. Measured SRO performance, with simulations superimposed. The quench voltage is a T_q- periodic pulse train given by (21) where $A_q = 0.9$ V, $B_q = -1.3$ V, and $T_q = 1/f_q$: (a) $f_q = 2$ MHz and (b) $f_q = 5$ MHz.

of the oscillator solution under constant time shifts: $x(t) \rightarrow x(t - nT_p)$, where n is an integer and T_p is the period of the RF input signal [30]. This implies one degree of freedom in the phase variable, which will affect both the oscillation-phase transient and its steady state. As a result, when describing the same system in two different manners, one can expect differences in the phase response $\phi(t)$. The circuit-level envelope transient and the two-band model are formally different systems with a different order. Thus, the oscillation phase will evolve in a different manner in each system. When the oscillation is extinguished, the system tends to the T_p- periodic solution forced by the RF input, and $\phi(t)$ becomes constant. One should note that, despite the described invariance, the oscillation phase can track the time variations of the input-signal phase $\phi(t)$, as shown in many previous works [4], [7], [8], [31], [32], [33], [34], [35]. Fig. 12 presents the phase of the output pulses when changing the phase of the RF input signal in steps of 45°. The results of the two-band model are compared with those obtained with circuit-level envelope transient. As can be seen, the phase is different during the oscillation pulses, in agreement with the above explanation, but becomes the same when the oscillation is off. In the two cases, the phase of the output pulses tracks the phase shifts of the input modulation.

IV. Experimental Results

For the experimental characterization, we have connected an Anritsu MG3710A vector signal generator (VSG) to the RF input of the SRO. The quench signal has been generated using a WW2572A arbitrary waveform generator, setting the dc offset voltage (V_{dc}) below the transistor threshold voltage. The output of the SRO has been connected to a spectrum analyzer and a digital storage oscilloscope (DSO90804A) through a power splitter (see Fig. 13).

The RF input frequency is $f_{in} = 2.7$ GHz and the input power is $P_{in} = -60$ dBm, which keeps the SRO output pulses above the noise floor. In the absence of the quench signal, the SRO is biased below the conduction threshold, with the gate voltage $V_{GG} = -1.3$ V and the drain voltage $V_{DD} = 0.7$ V. In the first test, we have considered the sinusoidal quench signal $v_q(t) = B_q + A_q \cos 2\pi f_q t$, with $B_q = -1.3$ V and $A_q = 0.9$ V, with three different quench frequencies: 2, 5, and 6 MHz. This choice will enable a clear evaluation of the progressive impact of the increase in the quench frequency on the output pulses. Fig. 14 shows the oscillator output voltage $v_{out}(t)$ obtained for each frequency. The results are compared with the amplitude $V_1(t)$ (at the fundamental frequency) provided by the two-band formulation of Section III. Because this formulation exhibited a good agreement with the circuit-level envelope transient, discrepancies are attributed to

modeling inaccuracies in the transistor and passive components. Nevertheless, in all cases, the effect on $v_{out}(t)$ is similar to the one obtained in Section III. In fact, the most valuable comparison is the one carried out versus circuit-level envelope transient since only in this case, we can be sure that the active and passive elements are identical. In comparison with the experimental results, inaccuracies in the component models will give rise to discrepancies that are not due to the simulation procedure, but to those modeling errors. For $f_q = 2$ MHz [Fig. 14(a)], the amplitude of the signal $v_{out}(t)$ grows up to 0.6 V during the oscillation intervals, in a manner like the simulation of Fig. 7. When the quench frequency increases to $f_q = 5$ MHz [Fig. 14(b)], the amplitude of the signal $v_{out}(t)$ grows up to 0.29 V only, and the length of the oscillation intervals decreases, in agreement with the simulation of Fig. 8. Finally, for the quench frequency $f_q = 6$ MHz, the oscillation is nearly extinguished, as predicted by the simulation of Fig. 9.

In a second test, we have introduced a rectangular quench signal of the form (21). We have considered two different values of the quench frequency: $f_q = 2$ MHz and $f_q = 6$ MHz. With the rectangular quench signal, the dynamic effects are observed from relatively low frequencies since the components of this multiharmonic signal are unevenly filtered by the baseband system. The impact of the increase of the quench frequency is similar to the one obtained with a sinusoidal waveform. The simulated and experimental output voltage $v_{out}(t)$ is represented in Fig. 15 for the two quench frequencies. For $f_q = 2$ MHz, the envelope of the output voltage $v_o(t)$ reproduces the square quench signal slightly filtered by the bias network, as in the simulation of Fig. 10. When the quench frequency increases to $f_q = 6$ MHz, the length of the oscillation intervals decreases, in agreement with the prediction of the simulations in Fig. 11. Again, because the new formulation exhibited a good agreement with the circuit-level envelope transient, discrepancies are attributed to inaccuracies in the models of the circuit components.

V. Conclusion

A two-band outer tier model of SROs in the envelope domain has been presented. It accounts for the oscillator circuitry at the oscillation band and at the quench-signal band. With the aid of this model, we have identified the baseband component that determines the oscillator stability properties under the variation of the quench frequency. When increasing the frequency, this baseband component becomes attenuated and delayed with respect to the quench signal, which explains dynamic effects that cannot be predicted with other models. The functions required by the formulation are easily extracted from HB by making use of two independent excitations, one in each of the two different bands. Once the model is available, it can be used for a system-level description of the SRO, as it can efficiently predict its response under arbitrary input modulations and choices of the frequency and shape of the quench signal. The developed model has been successfully tested through its application to an SRO at 2.8 GHz, which has been manufactured and experimentally characterized.

References

[1] F. W. Frink, "The basic principles of super-regenerative reception," *Proc. IRE*, vol. 26, no. 1, pp. 76–106, Jan. 1938.

[2] F. X. Moncunill-Geniz, P. Pala-Schonwalder, and O. Mas-Casals, "A generic approach to the theory of superregenerative reception," *IEEE Trans. Circuits Syst. I, Reg. Papers*, vol. 52, no. 1, pp. 54–70, Jan. 2005.

[3] M. Vossiek and P. Gulden, "The switched injection-locked oscillator: A novel versatile concept for wireless transponder and localization systems," *IEEE Trans. Microw. Theory Techn.*, vol. 56, no. 4, pp. 859–866, Apr. 2008.

[4] P. Pala-Schönwälder, J. Bonet-Dalmau, F. X. Moncunill-Geniz, F. del Águila-López, and R. Giralt-Mas, "A superregenerative QPSK receiver," *IEEE Trans. Circuits Syst. I, Reg. Papers*, vol. 61, no. 1, pp. 258–265, Jan. 2014.

[5] F. X. Moncunill-Geniz, J. Bonet-Dalmau, F. Del Aguila-Lopez, I. Demirkol, and P. Pala-Schonwalder, "Super-regenerative receiver for OFDM communication," in *Proc. IEEE Int. Symp. Circuits Syst. (ISCAS)*, Nov. 2022, pp. 1843–1847.

[6] H. Ghaleb et al., "A 180-GHz super-regenerative oscillator with up to 58 dB gain for efficient phase and amplitude recovery," *IEEE Trans. Microw. Theory Techn.*, vol. 68, no. 6, pp. 2011–2019, Jun. 2020.

[7] H. Ghaleb, P. V. Testa, S. Schumann, C. Carta, and F. Ellinger, "A 160-GHz switched injection-locked oscillator for phase and amplitude regenerative sampling," *IEEE Microw. Wireless Compon. Lett.*, vol. 27, no. 9, pp. 821–823, Sep. 2017.

[8] M. Vossiek, T. Schafer, and D. Becker, "Regenerative backscatter transponder using the switched injection-locked oscillator concept," in *IEEE MTT-S Int. Microw. Symp. Dig.*, Jun. 2008, pp. 571–574.

[9] A. Ferschischi, H. Ghaleb, C. Carta, and F. Ellinger, "61.5-GHz energy-efficient super-regenerative oscillator with tunable quench duty cycle," in *IEEE MTT-S Int. Microw. Symp. Dig.*, Jun. 2022, pp. 661–664.

[10] Y. Yuan, A. Y. Chen, and C. M. Wu, "Super-regenerative oscillator-based high-sensitivity radar architecture for motion sensing and vital sign detection," *IEEE Trans. Microw. Theory Techn.*, vol. 69, no. 3, pp. 1974–1984, Mar. 2021.

[11] Y. Yuan and C. M. Wu, "Multi-target concurrent vital sign and location detection using super-regenerative oscillator-based metamaterial pulsed radar," in *IEEE MTT-S Int. Microw. Symp. Dig.*, Jun. 2022, pp. 951–954.

[12] Y. Yuan and C. M. Wu, "Super-regenerative oscillator integrated metamaterial leaky wave antenna for multi-target vital sign and motion detection," *IEEE J. Electromagn., RF Microw. Med. Biol.*, vol. 6, no. 2, pp. 238–245, Jun. 2022.

[13] J. Bonet-Dalmau, F. X. Moncunill-Geniz, P. Pala-Schonwalder, F. del Aguila-Lopez, and R. Giralt-Mas, "Frequency domain analysis of superregenerative receivers in the linear and the logarithmic modes," *IEEE Trans. Circuits Syst. I, Reg. Papers*, vol. 59, no. 5, pp. 1074–1084, May 2012.

[14] L. A. Zadeh, "Frequency analysis of variable networks," *Proc. IRE*, vol. 38, no. 3, pp. 291–299, Mar. 1950.

[15] F. Ramirez, A. Suarez, I. Lizarraga, and J.-M. Collantes, "Stability analysis of nonlinear circuits driven with modulated signals," *IEEE Trans. Microw. Theory Techn.*, vol. 58, no. 4, pp. 929–940, Apr. 2010.

[16] S. Hernández and A. Suárez, "Envelope-domain analysis and modeling of super-regenerative oscillators," *IEEE Trans. Microw. Theory Techn.*, vol. 66, no. 8, pp. 3877–3893, Aug. 2018.

[17] E. Ngoya and R. Larcheveque, "Envelop transient analysis: A new method for the transient and steady state analysis of microwave communication circuits and systems," in *IEEE MTT-S Int. Microw. Symp. Dig.*, San Francisco, CA, USA, Jun. 1996, pp. 1365–1368.

[18] N. B. Carvalho, J. C. Pedro, W. Jang, and M. B. Steer, "Simulation of nonlinear RF circuits driven by multi-carrier modulated signals," in *IEEE MTT-S Int. Microw. Symp. Dig.*, Long Beach, CA, USA, Jun. 2005, pp. 801–804.

[19] S. Hernández and A. Suárez, "Analysis of superregenerative oscillators in nonlinear mode," *IEEE Trans. Microw. Theory Techn.*, vol. 67, no. 6, pp. 2247–2258, Jun. 2019.

[20] A. Soury, E. Ngoya, and J. M. Nebus, "A new behavioral model taking into account nonlinear memory effects and transient behaviors in wideband SSPAs," in *IEEE MTT-S Int. Microw. Symp. Dig.*, Dec. 2002, pp. 853–856.

[21] S. Sancho, S. Hernández, and A. Suárez, "Noise analysis of super-regenerative oscillators in linear and nonlinear modes," *IEEE Trans. Microw. Theory Techn.*, vol. 67, no. 12, pp. 4955–4965, Dec. 2019.

[22] A. Suarez, *Analysis and Design of Autonomous Microwave Circuits*. Hoboken, NJ, USA: Wiley, 2009.
[23] K. Kundert, "Introduction to RF simulation and its application," in *Proc. IEEE Bipolar/BiCMOS Circuits Technol. Meeting*, Minneapolis, MN, USA, Sep. 1998, pp. 67–78.
[24] K. S. Kundert, "Introduction to RF simulation and its application," *IEEE J. Solid-State Circuits*, vol. 34, no. 9, pp. 1298–1319, Sep. 1999.
[25] S. Sancho, F. Ramírez, and A. Suárez, "Stochastic analysis of cycle slips in injection-locked oscillators and analog frequency dividers," *IEEE Trans. Microw. Theory Techn.*, vol. 62, no. 12, pp. 3318–3332, Dec. 2014.
[26] K. Kurokawa, "Some basic characteristics of broadband negative resistance oscillator circuits," *Bell Syst. Tech. J.*, vol. 48, no. 6, pp. 1937–1955, Jul. 1969.
[27] V. Rizzoli, F. Mastri, A. Costanzo, and E. Montanari, "Highly efficient envelope-oriented analysis of large autonomous RF/microwave systems by a trust-region algorithm coupled with Krylov-subspace harmonic-balance," in *Proc. 32nd Eur. Microw. Conf.*, Oct. 2002, pp. 1–4.
[28] J. Jugo, J. Portilla, A. Anakabe, A. Suarez, and J. M. Collantes, "Closed-loop stability analysis of microwave amplifiers," *Electron. Lett.*, vol. 37, no. 4, p. 226, 2002.
[29] S. Ver Hoeye, A. Suarez, and S. Sancho, "Analysis of noise effects on the nonlinear dynamics of synchronized oscillators," *IEEE Microw. Wireless Compon. Lett.*, vol. 11, no. 9, pp. 376–378, Sep. 2001.
[30] S. Wiggins, *Introduction to Applied Nonlinear Dynamical Systems and Chaos*. New York, NY, USA: Springer-Verlag, 2003.
[31] R. Mirzalou and M. F. Wagdy, "An 8-PSK super regenerative receiver with new phase detection technique," in *Proc. 12th Int. Comput. Eng. Conf. (ICENCO)*, Dec. 2016, pp. 14–19.
[32] G. H. Ibrahim and A. N. Hafez, "An 8-PSK digital phase detection technique for super-regenerative receivers," in *Proc. IEEE Int. Conf. Electron., Circuits, Syst. (ICECS)*, Dec. 2015, pp. 240–243.
[33] D. Lee and P. P. Mercier, "Noise analysis of phase-demodulating receivers employing super-regenerative amplification," *IEEE Trans. Microw. Theory Techn.*, vol. 65, no. 9, pp. 3299–3311, Sep. 2017.
[34] S. Saleh and G. Hamdy, "A comparative study of super-regenerative receivers for BAN applications," *Int. J. Microelectron. Comput. Sci.*, vol. 8, no. 4, pp. 133–138, 2017.
[35] H. Ghaleb, C. Carlowitz, D. Fritsche, C. Carta, and F. Ellinger, "A 180-GHz super-regenerative oscillator with up to 58 dB gain for efficient phase recovery," in *Proc. IEEE Radio Freq. Integr. Circuits Symp. (RFIC)*, Jun. 2019, pp. 131–134.

Sergio Sancho (Senior Member, IEEE) received the Licentiate degree in physics from Basque Country University, in 1997, and the Ph.D. degree in electronic engineering from the University of Cantabria, Santander, Spain, in 2002.

In 1998, he joined the Communications Engineering Department, University of Cantabria, where he currently works as an Associate Professor with the Communications Engineering Department. His research interests include the nonlinear analysis of microwave autonomous circuits and frequency synthesizers, including stochastic and phase-noise analysis.

Almudena Suárez (Fellow, IEEE) was born in Santander, Spain. She received the Licentiate degree in electronic physics and the Ph.D. degree from the University of Cantabria, Santander, in 1987 and 1992, respectively, and the Ph.D. degree in electronics from the University of Limoges, Limoges, France, in 1993.

She is currently a Full Professor with the University of Cantabria, where she is also the Head of the Microwave Engineering and Radiocommunication Systems Research Group. She has authored the book *Analysis and Design of Autonomous Microwave Circuits* (IEEE-Wiley, 2009) and has coauthored the book *Stability Analysis of Nonlinear Microwave Circuits* (Artech House, 2003).

Prof. Suárez is a member of the TPCs of IEEE International Microwave Symposium and European Microwave Week. She was a member of the Board of Directors of European Microwave Association (EuMA) from 2012 to 2020. She has been the Publication Officer of EuMA since 2021. She received the Research Award of the Social Council of the University of Cantabria in 2021. She was an IEEE Distinguished Microwave Lecturer from 2006 to 2008. She was the Coordinator of the Communications and Electronic Technology Area for the Spanish National Evaluation and Foresight Agency (ANEP) from 2009 to 2013. She was the Chair of the 2014 and 2015 editions of IEEE Topical Conference on RF/Microwave Power Amplifiers (PAWR) in Newport Beach, CA, USA, and San Diego, CA. She was the General TPC Chair of EuMW 2018. She was the Editor-in-Chief of the *International Journal of Microwave and Wireless Technologies* from Cambridge University Press journals from 2013 to 2018 and is currently an Associate Editor of *IEEE Microwave Magazine* and the Editor-in-Chief of IEEE TRANSACTIONS ON MICROWAVE THEORY AND TECHNIQUES. She has been the Chair of the IEEE Subcommittee for the Best Paper Award in *IEEE Microwave Magazine* since 2017.

Franco Ramírez (Senior Member, IEEE) received the Licentiate degree in electronic systems engineering from the Military School of Engineering (EMI), La Paz, Bolivia, in 2000, and the Ph.D. degree in communications engineering from the University of Cantabria, Santander, Spain, in 2005.

From 1999 to 2000, he worked with Ericsson de Bolivia Telecomunicaciones, La Paz, where he was involved in projects related with global system for mobile communications (GSM) and time-division multiple access (TDMA) technologies. From 2009 to 2013, he was a Research Fellow of the "Ramón y Cajal" Programme, funded by the Spanish Ministry of Science and Innovation, with the Communications Engineering Department, University of Cantabria, where he is currently an Associate Professor. His research interests include phase noise, stability, and the development of nonlinear techniques for the analysis and design of autonomous microwave circuits.